Differential interference contrast x-ray microscopy with twin zone plates

Burkhard Kaulich

X-Ray Microscopy Section, ELETTRA–Sincrotrone Trieste, S.S.14, km 163.5 in Area Science Park, I-34012 Basovizza-Trieste, Italy

Thomas Wilhein

RheinAhrCampus Remagen, University of Applied Sciences, Suedallee 2, D-53424 Remagen, Germany

Enzo Di Fabrizio, Filippo Romanato, and Matteo Altissimo

TASC-INFM at ELETTRA–Sincrotrone Trieste, S.S.14, km 163.5 in Area Science Park, I-34012 Basovizza-Trieste, Italy

Stefano Cabrini

Instituto di Elletronica della Stato Solido, Via Cineto Romano 42, 00158 Rome, Italy

Barbara Fayard and Jean Susini

ID21 X-Ray Microscopy Beamline, European Synchrotron Radiation Facility, BP 220, F-34073 Grenoble Cedex, France

Received May 14, 2001; revised manuscript received August 27, 2001; accepted September 12, 2001

X-ray imaging in differential interference contrast (DIC) with submicrometer optical resolution was performed by using a twin zone plate (TZP) setup generating focal spots closely spaced within the TZP spatial resolution of 160 nm. Optical path differences introduced by the sample are recorded by a CCD camera in a standard full-field imaging and by an aperture photodiode in a standard scanning transmission x-ray microscope. Applying this x-ray DIC technique, we demonstrate for both the full-field imaging and scanning x-ray microscope methods a drastic increase in image contrast (approximately 20×) for a low-absorbing specimen, similar to the Nomarski DIC method for visible-light microscopy. © 2002 Optical Society of America

OCIS codes: 180.7460, 340.7450, 180.3170, 180.5810, 340.6720.

1. INTRODUCTION

The discovery of x rays by Roentgen[1] in 1865 demonstrated immediately their penetration power, which is of still growing importance for all fundamental and applied fields of research. From the need for higher optical resolution than that in projection imaging emerged the idea of soft-x-ray microscopy using photon energies between the C and O absorption edges.[2] With the development of x-ray microscopes[3–7] at second- and third-generation electron storage ring facilities, it became clear that the employment of contrast techniques using the real, phase-shifting part of the refractive index is of importance for mainly two reasons: (1) The employment of phase contrast techniques can lead to a tremendous reduction of the x-ray dose applied to a specimen.[8–10] (2) Away from element absorption edges, phase shift is dominating with increasing photon energy, especially for multi-keV and hard x rays.

A phase contrast technique for full-field imaging microscopy was first outlined for soft x rays by Schmahl *et al.*,[11,12] who used, analogous to the Zernike-type phase contrast setup[13] for visible light, a phase-shifting plate in the back focal plane of the objective zone plate (ZP). In scanning-type microscopes, a variety of techniques have been used to detect the differential phase response of the specimen refracted light. Morrison *et al.*[14,15] and Chapman *et al.*[16] demonstrated differential phase contrast and dark-field imaging using a CCD camera[17,18] to collect the entire two-dimensional pattern for each pixel of the raster scan in the far field of the specimen. Polack *et al.*[19] and Joyeux *et al.*[20] proposed and carried out experiments on x-ray differential interference contrast (DIC) using a Young's-type slit setup in combination with a configured detector. Davis *et al.*[21,22] proved differential phase contrast by using double-crystal optics in the hard-x-ray range. The development of highly coherent third-generation synchrotron radiation sources made a variety of phase contrast techniques possible, including holography and phase contrast tomography.[23–30]

Our purpose in this work is to demonstrate the feasibility of x-ray DIC generated by a twin zone plate (TZP) setup. The use of two ZP setups for visible-light

 © 2002 Optical Society of America

interferometry,[31–33] metrology,[34–36] and optical sensing[37] dates back to a few decades ago. The principle of using TZPs for interferometry with multi-keV x rays was described recently.[38]

The appeal of this contribution arises from recently achieved advances in lithography and nanostructuring techniques,[39] which made it possible to generate special TZPs for multi-keV x rays. The ZPs are transverse to the optical axis and displaced in the order of their optical resolution of approximately 200 nm, which also means that the Airy disks of their focal spots are displaced within the optical resolution. Thus the wave-front division by the TZP can be used for differential imaging with x rays, intrinsically taking advantage of the high optical resolution achievable with ZPs.[40]

We can anticipate the following advantages of using a TZP for x-ray DIC imaging: (1) The alignment of the TZP is comparatively uncomplicated and similar to that of a single ZP. (2) This DIC technique is usable for both complementary x-ray imaging techniques, i.e., the full-field imaging and scanning types. (3) The images are online visible. (4) Because of small shear of the wave-front division and small optical path differences, this method makes no use of coherence of the x-ray beam and can also be used with incoherent sources. Indeed, a ZP requires monochromatic light for diffraction-limited imaging given by $E/\Delta E \geqslant N$, where E is the photon energy and N is the number of zones.

We focus in Section 2 on imaging properties and characterization of the TZPs for differential imaging. In Section 3, we describe and discuss experiments performed with x-ray microscopes at the ID21 beamline[41] of the European Synchrotron Radiation Facility (ESRF).[42] In Section 4, we discuss and conclude the experimental results.

2. IMAGE FORMATION WITH THE TWIN ZONE PLATE

ZPs are circular diffraction gratings with radially increasing line density that generate focal spots given by[43]

$$f_m = 2r\Delta r/(\lambda m) = r^2/(\lambda N m), \tag{1}$$

where λ denotes the wavelength, f_m is the focal length in the mth diffraction order, Δr is the outer zone width, r is the radius of the ZP, and N is the total number of zones. Thus ZPs have, as expected from the diffraction principle, an infinite number of foci. The spot size δ_m in the mth-order focused beam is determined by its diffraction-limited resolution $\delta_{i,m}$ given by the numerical aperture of the optic, the geometrical demagnified source size δ_r, and the chromatic aberration δ_c:

$$\begin{aligned}\delta_m &= [\delta_{i,m}^2 + \delta_r^2 + \delta_c^2]^{1/2} \\ &= [(1.22\Delta r/m)^2 + \delta_r^2 + (D\Delta E/E)^2]^{1/2},\end{aligned} \tag{2}$$

where D equals the diameter of the ZP and $\Delta E/E$ is the energy resolution of the monochromator. δ_r^2 is a function depending on the geometry of the setup. For a scanning-type microscope, it equals $(\sigma q/p)^2$, where σ is the source size, p is the source-to-ZP distance, and q is the ZP-to-sample distance. For the full-field imaging type, it is a function of the detector geometry and its pixel size Δ_p: $\delta_r = \Delta_p/(Vm)$, where V is the magnification of the image by the objective ZP.[44]

The depth of focus (DOF) of a ZP in the +1 diffraction order is given by

$$\mathrm{DOF} = \pm 2\Delta r^2/\lambda. \tag{3}$$

A. Interferometry with a Twin Zone Plate

A ZP splits an incident plane wave into a (zero-order) plane wave and a set of spherical waves (± 1 and higher orders). A second ZP placed close to the first one interacts with x rays coming from the first ZP and generates an additional set of plane and spherical waves that can interfere with the wave fronts of the first ZP. The complex situation of interference of all these waves is shown in Fig. 1, where (n, m) denotes the interference of order n of the first ZP and order m of the second ZP.

Assuming that spurious diffraction orders higher than +1 are blocked by an order-sorting aperture, only four waves [(0, 0), (1, 0), (0, 1), and (1, 1)] propagate in the image space. Relevant for the DIC image formation are the combinations (1, 0) and (0, 1). (0, 0) can be blocked by a central stop close to the image plane, and (1, 1) can be blocked in a scanning-type microscope by an order-sorting aperture downstream of the TZP. In the case of a full-field imaging microscope (TXM), (1, 1) cannot be easily removed and gives a weak background signal. (0, 1) and (1, 0) generate an interference pattern, which is superposed onto the absorption contrast image.

Shape, distance, and orientation of fringes depend strongly on the displacement vector $(\Delta x, \Delta y, \Delta z)$ of the two ZPs. For the relevant case of a pure, in-plane displacement perpendicular to the optical axis with $\Delta_z = 0$, a fringe pattern of nearly straight lines is observed, which is described, with (x, y, z) as coordinates in the recording plane and s as an integer, by[45]

$$(\Delta_x/z)x + (\Delta_y/z)y = s\lambda. \tag{4}$$

The distance D between neighboring lines is equal to

$$D = \lambda z/(\Delta_x^2 + \Delta_y^2)^{1/2}, \tag{5}$$

where $z = 0$ is located in the back focal plane of the TZP.

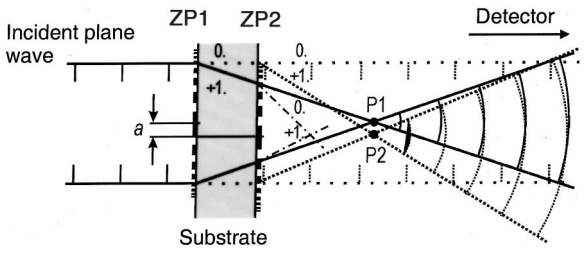

Fig. 1. X-ray interference imaging with a twin zone plate (TZP). Beam splitting accomplished by ZP1 and ZP2 generates four waves in the image space. Apertures (not shown) block all combinations of diffraction orders other than (0, 1) and (1, 0), resulting in interference of two spherical waves originating from P1 and P2. The lateral displacement of P1 and P2 is of the same value, a, as that denoting the spacing of ZP1 and ZP2.

Thus an interference pattern generated by a TZP allows for complete control of fringe orientation and spacing if it is possible to control the distance vector between both ZPs with sufficient accuracy.

B. Differential Interference Imaging with a Twin Zone Plate

Differential imaging means that the lateral image separation is smaller than the optical resolution of the imaging optics or, in terms of a scanning probe geometry, that the distance of the maxima of the Airy disks of both ZPs is smaller than their optical resolution.

With use of the full-field imaging geometry as described below, the image field $\oslash_I$ is given by $\oslash_I = \oslash_p z/f$, where the diameter of the order-sorting aperture is $\oslash_p$. Assuming for simplicity that the ZPs are displaced only in the x direction, the condition for the necessary displacement can be described as

$$\Delta x < 2r\Delta r/\oslash_p . \tag{6}$$

ZP imaging fulfills this condition when the lateral displacement of the two ZPs is of the order of the outermost zone width Δr.

In addition, the separation Δz of the ZPs along the optical axis has to be well within the DOF. Otherwise, two differently sized images would be observed. According to Eq. (3), this leads to the condition

$$\Delta z < 4\Delta r^2/\lambda . \tag{7}$$

C. Coherence Considerations

To understand why DIC imaging with ZPs in the described geometry setup works, one has to consider the requirements that this method places on both spatial and temporal coherence of the light source.

1. Spatial Coherence

The van Cittert–Zernike theorem applied to the case of a circular light source of diameter d located a distance L from a plane of observation gives a limit for the coherently illuminated field D (Ref. 46):

$$D = 0.61\frac{L\lambda}{d/2}. \tag{8}$$

On the other hand, the spatial resolution of a ZP is, according to the Rayleigh criterion, determined by $\delta = 1.22\Delta r$ [from Eq. (2), considering an ideal point source and negligible monochromatic aberration].

Figure 2 illustrates the situation for microscope imaging. If we consider the object plane as being composed of small sources with diameter $d = \delta$, each such element will in a first-order approximation produce a diffraction-limited image in the image plane. For large magnifications, $L \approx f$, and using Eqs. (1) and (8) gives

$$D = 2r. \tag{9}$$

The diameter of the coherently illuminated field equals the diameter of the ZP. Thus a ZP is coherently illuminated by a source with a diameter corresponding to the diffraction-limited resolution element of the ZP itself. In other words, a light source that is an Airy pattern generated by diffraction-limited optics is intrinsically coherent. This statement is not limited to ZPs but holds for all types of imaging optics. Applied to DIC imaging, the derived results mean that if the separation of the two superimposed images is below the resolution limit, i.e.,

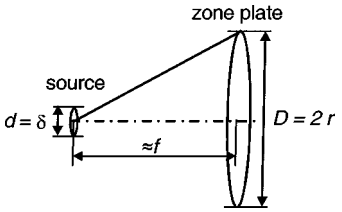

Fig. 2. The limit for a spatially coherent illuminated field D equals the ZP diameter $2r$ when the source diameter d is given by the spatial resolution δ, assuming that the illuminating source is located close to the front focal plane (as for microscopy).

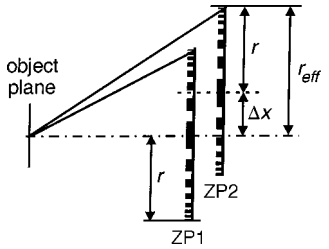

Fig. 3. Illustration of effective radius r_{eff} of a TZP for calculations of desired monochromaticity and temporal coherence. ZP1 (ZP2) = first (second) ZP, for interference contrast x-ray microscopy, r = radius of the two identical ZPs, and Δx = lateral shift of the ZPs.

$$\Delta x < \delta = 1.22\Delta r, \tag{10}$$

where Δx denotes the shift with respect to the image plane, then one can understand that the two images will interfere without further considerations or restrictions to the spatial coherence properties of the illuminating source. The essential information given by relation (10) is that interferometric operation in differential imaging will not be affected by the degree of spatial coherence delivered by the illumination.

The described experiments were carried out by using a TZP having a shift $\Delta x \approx \Delta r/2$, so that the necessary conditions concerning differential imaging and spatial coherence are fulfilled.

2. Temporal Coherence

Because of the fact that the image-forming process is diffraction when ZPs are used for imaging, the focal length is a function of the wavelength [see Eq. (1)], which can be treated as a strong monochromatic aberration. Figure 3 shows Fresnel's zone construction and can be used to explain the monochromaticity necessary for diffraction-limited ZP imaging.

Assuming a point on the optical axis as object, the shortest optical path from object plane to image plane is that along the optical axis. All other paths show an additional length given by $(\lambda/2)$ times zone number. Hence the maximum path-length difference $\Delta s_{\max}$ is

$$\Delta s_{\max} = \frac{\lambda}{2} N, \tag{11}$$

where N denotes the total number of zones. The additional optical path-length differences introduced by the specimen's structure is negligible in terms of coherence considerations for almost all objects in x-ray microscopy: Assuming a typical object thickness ($\approx 10\ \mu$m) and variation of the real part of the refractive index ($\approx 10^{-4}$) leads to optical path-length differences in the nanometer range, corresponding to a few wavelengths, which is small compared with the number resulting from the monochromaticity desired for ZP imaging. For the observation of constructive interference of light coming from all zones in the image plane, the condition for the coherence length l_{coh} of the illuminating light is

$$l_{\mathrm{coh}} \geqslant \Delta s_{\max}. \tag{12}$$

If we consider the general formula $l_{\mathrm{coh}} = \lambda^2/(2\Delta\lambda)$ for the coherence length, where $\Delta\lambda$ denotes the FWHM of the spectral distribution, Eq. (11) for the maximum path-length difference results in

$$l_{\mathrm{coh}} = \frac{\lambda^2}{2\Delta\lambda} \geqslant \frac{\lambda}{2} N = \Delta s_{\max}, \tag{13}$$

which finally gives

$$\frac{\lambda}{\Delta\lambda} \geqslant N \tag{14}$$

(cf. Ref. 38). For example, the monochromaticity that has to be achieved by an appropriate monochromator should at least be as high as the number of zones. For interference imaging with two ZPs, the lateral displacement of the ZPs leads to further constraints. In the above given model, calculations for time-coherent illumination of two ZPs shifted with respect to each other have to take into consideration all parts of both ZPs. In the case of two ZPs with equal radius r and small distance along the optical axis, an effective radius r_{eff} may be introduced. From Fig. 3, it can be derived that here r_{eff} is

$$r_{\mathrm{eff}} = r + \Delta x. \tag{15}$$

The number of zones N and the radius r of a ZP are related by[44]

$$N = \frac{r^2}{\lambda f}. \tag{16}$$

In a first-order approximation, this gives

$$N_{\mathrm{eff}} = \frac{r_{\mathrm{eff}}^2}{\lambda f} = \frac{(r + \Delta x)^2}{\lambda f} \tag{17}$$

for the effective zone number N_{eff} and

$$\Delta N = N_{\mathrm{eff}} - N = \frac{(2r + \Delta x)\Delta x}{\lambda f} \tag{18}$$

for the number of additional zones. In practical cases, one can assume that $r \gg \Delta x$, so that

$$\Delta N \approx \frac{2r\Delta x}{\lambda f}. \tag{19}$$

For differential imaging, $\Delta x \leqslant \Delta r$, and Eq. (1) and relation (19) give for a maximum value $\Delta x = \Delta r$ the relation

$$\Delta N \approx 1, \tag{20}$$

which is obvious from a geometrical point of view if one treats the two ZPs as being located in the same plane perpendicular to the optical axis. The effective zone number N_{eff}, which determines the requirements of DIC imaging to the temporal coherence and thus the monochromaticity of the illumination, is

$$N_{\mathrm{eff}} = N + \Delta N = N + 1 \approx N. \tag{21}$$

The approximation $N + 1 \approx N$ assumes large zone numbers, which is valid for typical ZPs implemented in x-ray microscopy, where N exceeds 100.

From the above given calculations, it can be stated that the requirements concerning temporal coherence needed for DIC with TZPs are satisfied when the monochromaticity of the illumination is sufficient for diffraction-limited imaging, that is, $\lambda/\Delta\lambda \geqslant N$. Thus no precautions with respect to the spectrum of the illuminating source other than those for "normal" ZP imaging have to be considered.

D. Generation and Image Performance of the Twin Zone Plate

Following the above considerations, we fabricated TZPs in Au with the following geometrical characteristics at a photon energy of 4 keV: 37.75 μm in radius, first-order focal length of 50 mm, outermost zone width of 200 nm, and zone height of 420 nm. The ZPs were built by electron-beam lithography and electroplating on both sides of a 1-μm-thick Si_3N_4 window. The nominal displacement of the two ZPs was less than 100 nm.

The theoretical first-order diffraction efficiency (that is, the fraction of the incoming light diffracted in the first order) of each ZP is 14%; the zero-order contribution is calculated to be 35%.

For the calculation of the total diffraction efficiency of the TZP, the zero-order transmissions of the two ZPs also have to be taken into account (zero order passing through the first ZP and diffracted in first order by the second ZP plus first order of the first ZP; that is, weakened by the zero-order transmission of the second ZP). The total diffraction efficiency η_{tot} can be expressed as

$$\eta_{\mathrm{tot}} = t_{\mathrm{ZP1}}\eta_{\mathrm{ZP2}} + t_{\mathrm{ZP2}}\eta_{\mathrm{ZP1}}, \tag{22}$$

where the transmission of the first (second) ZP is t_{ZP1} (t_{ZP2}) and the diffraction efficiency of the first (second) ZP is η_{ZP1} (η_{ZP2}).

This consideration is based on the fact that the diffraction of both ZPs can be treated as independent. The measured first-order diffraction efficiency of the TZP is 9.6% at 4 keV, which is close to the theoretically expected value. The efficiency value was acquired by measuring the first-order flux through an aperture in the back focal plane of the TZP and normalizing it with the flux through an aperture with the same diameter as that of the TZP.

The optical resolution was measured by imaging a W Siemens star with a full-field imaging microscope (TXM)

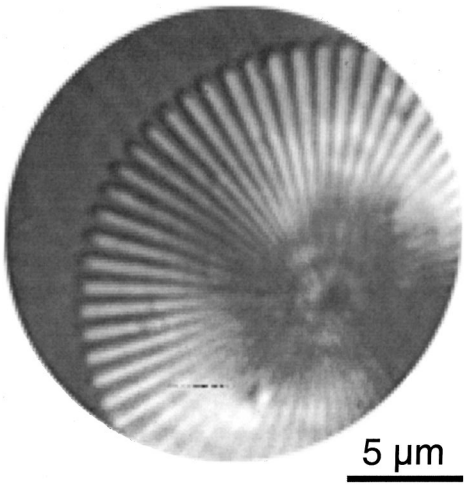

Fig. 4. X-ray image of a W Siemens star taken with the full-field imaging microscope (TXM) in differential interference contrast (DIC) mode. The Siemens star with 20-μm diameter and 36 spokes with line widths varying from 2 to 0.1 μm served as a test specimen to measure the optical resolution. Periods of 320 nm could be resolved.

(see Subsection 3.A). The Siemens star is 20 μm in diameter and 300 nm in thickness and has 36 spokes with line widths varying from 2 μm down to 0.1 μm. From the x-ray image shown in Fig. 4, periods of approximately 320 nm could be resolved.

3. DIFFERENTIAL INTERFERENCE MICROSCOPY WITH MULTI-keV PHOTONS

The experiments were performed at the ID21 x-ray microscopy beamline[41] at the ESRF. The x-ray beam at this beamline is generated by a 1.6-m-long, 42-mm-period undulator, which is here used at a photon energy of 4 keV. With an undulator K value of 1.45, the measured integrated flux is 7×10^{11} photons s^{-1} $(Si\langle 111\rangle BW)^{-1}$ $(200\ mA)^{-1}$ at a beam size of 0.5 mm $\times$ 0.5 mm. The x-ray source size (FWHM) at this photon energy is 140 μm horizontally and 24 μm vertically.

The beam is preconditioned by two bounce reflections from two parallel, horizontally deflecting Ni-coated mirrors. At a glancing angle of 8 mrad, the Ni reflections give a cutoff energy of 10 keV. This gives a total harmonic suppression for 12-keV photons (third harmonic) of better than 10^3 and greatly reduces the incident power on the downstream optical components. Contributions of the second harmonic at 8 keV are suppressed by a Si$\langle 111\rangle$ crystal monochromator. The bremsstrahlung and scattered radiation is separated from the offset undulator radiation by passage through a narrow hole in a tungsten block in combination with a collimator. This allows for a tremendous reduction of downstream radiation shielding and offers relatively free access to the microscope during experiments.

The ID21 beamline houses two x-ray microscopes on two independent branch lines: a scanning x-ray microscope (SXM) on the direct branch and a full-field imaging microscope (TXM) on a side branch. Both microscopes were used for proving the feasibility of DIC with TZPs at 4-keV photon energy.

A. Differential Interference Contrast X-Ray Imaging with a Full-Field Imaging Microscope

The full-field imaging microscope, or TXM, works similarly to a visible-light transmission microscope, despite the fact that ZPs are used as focusing optics: The x-ray beam is monochromatized by a Si crystal monochromator with an energy resolution of 0.7 eV at a photon energy of 4 keV.[47] A condenser ZP focuses the x-ray beam onto the sample. A high-optical-resolution ZP downstream of the sample then generates a magnified image onto a CCD camera. When the TXM is operated in DIC mode (see Fig. 5a), the TZP is placed as the imaging objective behind the sample and (0, 1) and (1, 0) wave fronts generate the image within the (0, 0) contribution of the condenser illu-

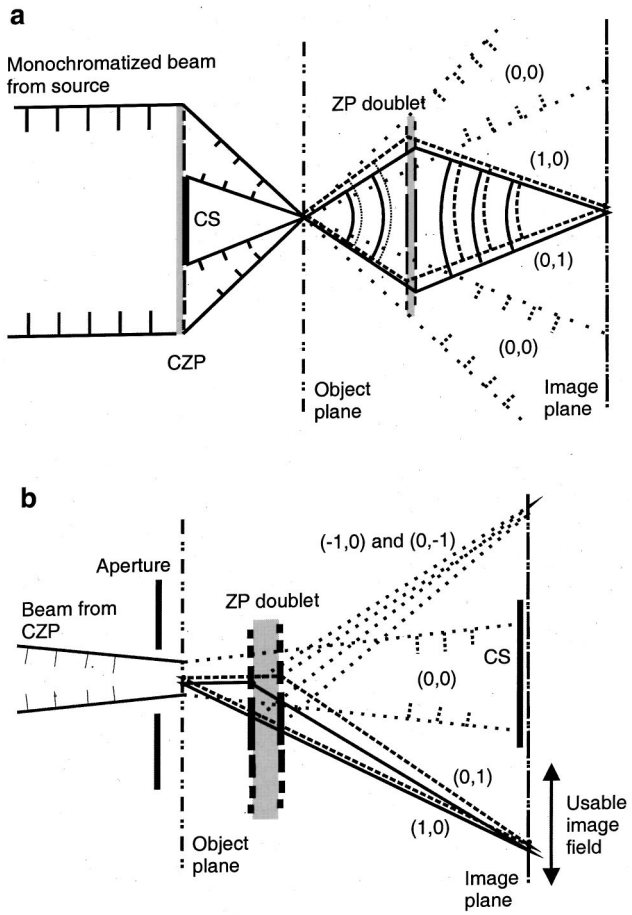

Fig. 5. a, Optical scheme of the TXM used for the x-ray DIC imaging at the ID21 x-ray microscopy beamline of the European Synchrotron Radiation Facility. The x-ray beam from the source is monochromatized by a Si crystal monochromator (not included in the sketch) and focused by a condenser optic onto the sample. The TZP upstream of the sample generates a magnified image, which is detected by a CCD camera. b, Because of the small numerical aperture of the condenser illumination, the +1-order image is overlapped with the −1-order projection. Therefore a pinhole is aligned slightly off axis close to the sample in order to separate the +1 and −1 order. CS stands for central stop, and CZP refers to the condenser ZP.

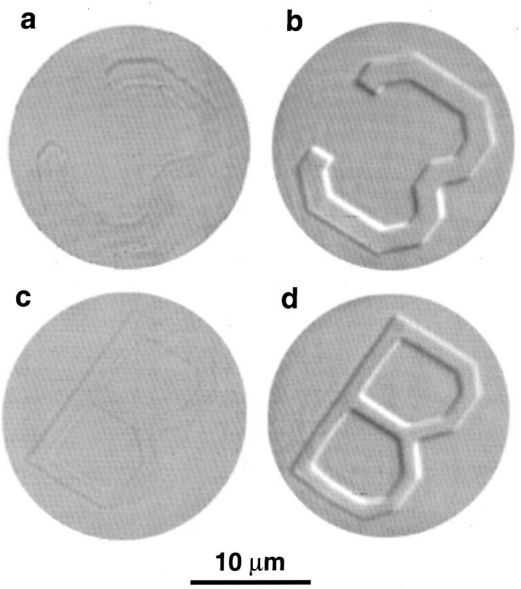

Fig. 6. Comparison of bright-field and DIC x-ray imaging. The images show 2-μm-thick poly(methyl methacrylate) (PMMA) test structures with 98.8% transmission at a photon energy of 4 keV. a, c, Bright-field images; b, d, DIC x-ray microscope images. Exposure time was 20 s, and field of view was 20 μm in diameter.

mination. Operation of the TXM with partially coherent or incoherent illumination in DIC mode is possible, as explained in Section 2.

The condenser ZP currently in use has a diameter of 1.2 mm, an outermost zone width $\Delta r_N = 826$ nm, and a focal length of 3630 mm. The measured photon flux in the focal spot at 4 keV is 3×10^8 photons s^{-1} (Si⟨111⟩BW) $(200\ \mathrm{mA})^{-1}$. Because of the mismatch of the numerical apertures of condenser and imaging objective and the small numerical aperture of the condenser, the +1-order image would be overlapped with the −1-order projection with slightly different magnification. Therefore an off-axis geometry was applied by introducing a 50-μm-diameter aperture off axis close to the sample, as shown in Fig. 5b, in order to separate the (+1, 0) and (0, +1) wave fronts from the (0, 0), (−1, 0), and (0, −1) wave fronts.[48] This introduces a weak, oblique illumination and limits the usable image field. (0, 0) contributions are blocked by a central stop close to the CCD, which was a Princeton CCD (EEV chip with 1340 × 1240 pixels and a pixel size of 20 μm × 20 μm) coupled by a two-stage visible-light optical system to a Gd_2O_2S:Tb powder phosphor screen with a thickness of 10 μm.[49,50]

As a good test object for phase-sensitive imaging at 4 keV, poly(methylmethacrylate) (PMMA) structures with a thickness $t = 2\ \mu$m are used. The phase-shifting, real part of these structures is, at a photon energy of 4 keV, 2 orders of magnitude higher ($\delta = 1.68 \times 10^{-5}$) than the absorbing, imaginary part ($\beta = 1.57 \times 10^{-7}$) of the refractive index $n = 1 - \delta - i\beta$. Taking into account that the transmission of PMMA is here 98.8%, one can expect an increase in contrast when the x-ray DIC technique is applied. The corresponding phase shift $\phi = (2\pi/\lambda)\delta t$ is 0.706 rad at 4-keV photon energy.

Figure 6 shows x-ray images documenting the drastic increase in image contrast when the x-ray DIC technique is applied (Figs. 6b and 6d) compared with that for absorption contrast imaging (Figs. 6a and 6c). The three-dimensional appearance (shadowing) of the structures is similar to that in differential interference imaging techniques for visible light on account of the directionality of the differential image shift. The intensity distribution caused by the DIC is visualized in the contour plot of Fig. 7a with ZPs displaced in the upper left to lower right direction. The line plot across the letter as shown in Fig. 7b demonstrates enhancement in image contrast when the optical path changes (here as a result of change in thickness at the edge of the structure).

Biological samples typically consist of elements with low atomic numbers and can therefore hardly be visualized with sufficient image contrast in absorption with multi-keV x rays. Figure 8 gives an example for the increase in image contrast for biological samples when the differential interference imaging is applied. The specimen was in this case a wing of a moth.

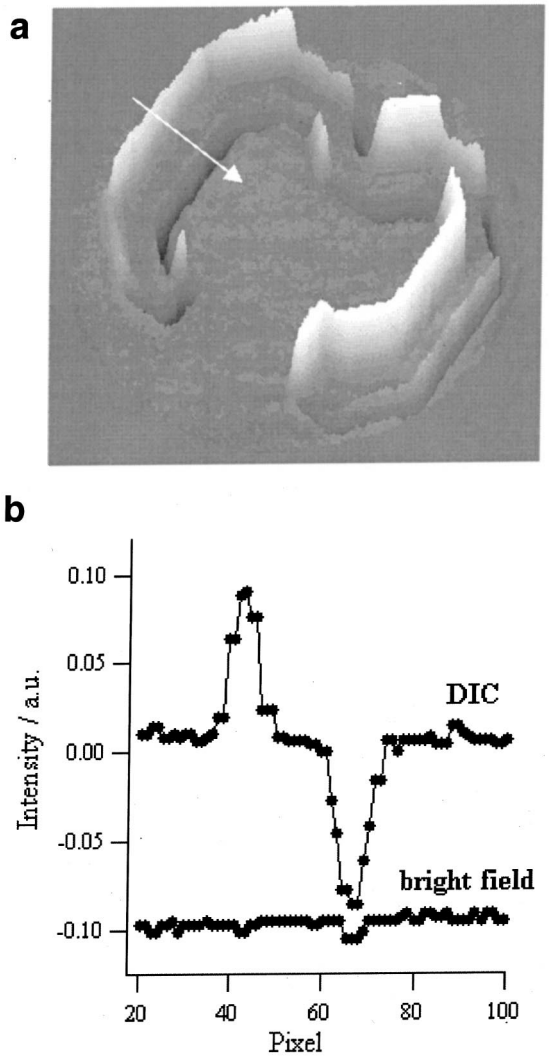

Fig. 7. a, Three-dimensional plot of the letter "3" in 2-μm-thick PMMA resist as shown in Fig. 6b, which was derived from the x-ray image in Fig. 6d. b, Line scan across the letter as indicated in a, demonstrating the edge enhancement, which is typical for DIC imaging. To demonstrate the increase in image contrast, we plotted a line scan through the image of the same test structure in bright-field or absorption contrast (see Fig. 6a).

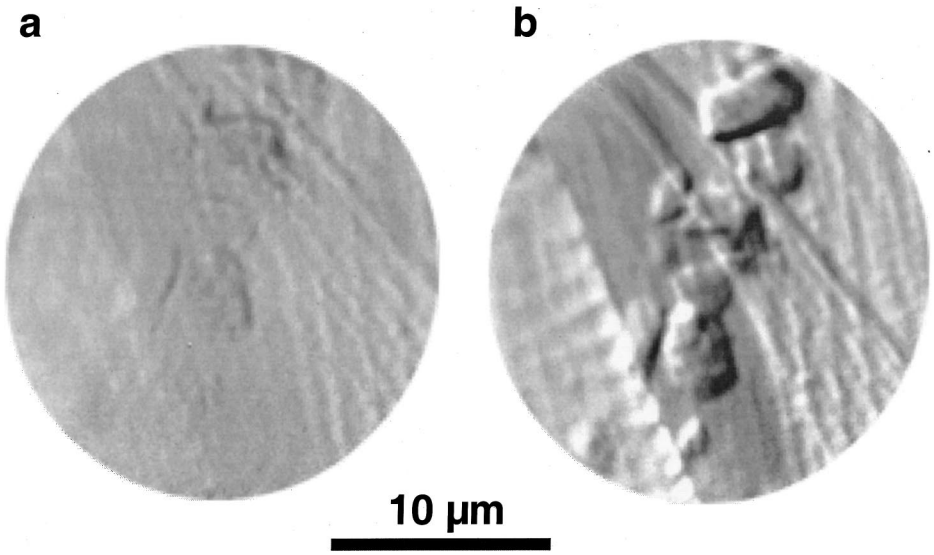

Fig. 8. a, Bright-field; b, x-ray DIC image showing microscopic details of a wing of a moth. Exposure time was 20 s, and field of view was 20 μm in diameter.

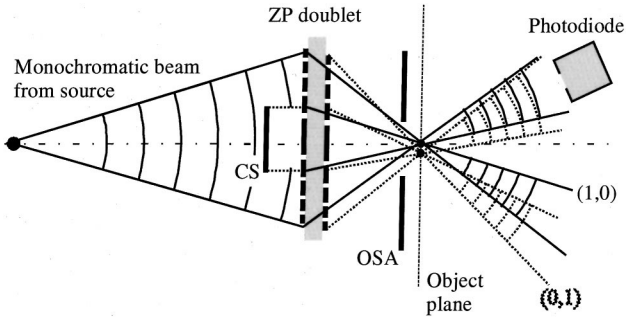

Fig. 9. Optical scheme of the scanning x-ray microscope (SXM) setup in DIC mode. CS is the central stop that blocks zero-order light, and OSA is the order-sorting aperture that blocks wave fronts other than (1, 0) and (0, 1).

B. Differential Interference Contrast Imaging with a Scanning X-Ray Microscope

In the scanning x-ray microscope (SXM), a single ZP forms a microprobe, and the sample is scanned across the probe. In the SXM, the optical resolution is a function of the diffraction-limited resolution of the ZP convoluted with functions describing the energy resolution and the finite source size of the x-ray beam [see Eq. (2)]. Thus the SXM configuration lends itself to the freedom of simultaneous use of different detectors.

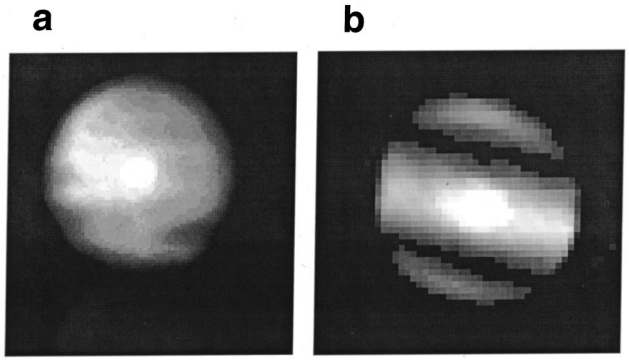

Fig. 10. a, Image of the +1 order of a single ZP. The image was acquired by raster-scanning a photodiode with a 50-μm aperture in front across the first-order cone of the single ZP. b, Corresponding image of the +1 order of the TZP with interference fringes that are due to the phase modulation by the two ZPs.

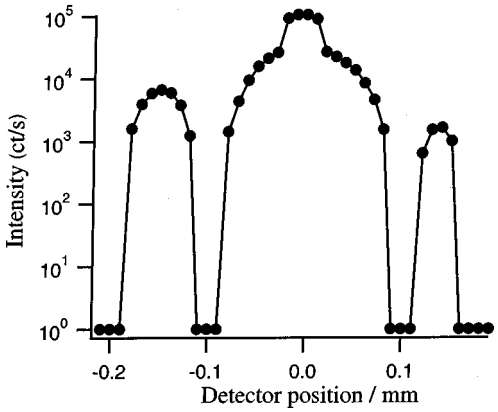

Fig. 11. Line scan across the interference fringes in the +1 order of the TZP related to Fig. 10. The amplitude difference between bright and dark parts of the interference pattern is more than 4 orders of magnitude. Intensity is given in units of counts per second.

Assuming that the image is formed entirely from the specimen attenuation at each pixel of the raster scan, the scanning transmission x-ray microscope delivers, similarly to the TXM, a bright-field image. This assumption is valid when the detector is large enough in diameter to integrate all light diffracted by the specimen.[51,52] The situation is different when a configured detector is used and only a part of the phase response of the sample is used for the image formation.

In the scanning transmission microscope setup[53] used at the ID21 beamline at the ESRF, the TZP was introduced at a distance of 53 m from the source. Monochromaticity of $\Delta E/E = 1 \times 10^{-4}$ was provided by a Si⟨111⟩ double-crystal monochromator. According to Eq. (2), the TZP forms two closely spaced diffraction-limited spots, which generate an interference pattern in the far-field detector plane, as shown in Fig. 9. A 10-μm-diameter

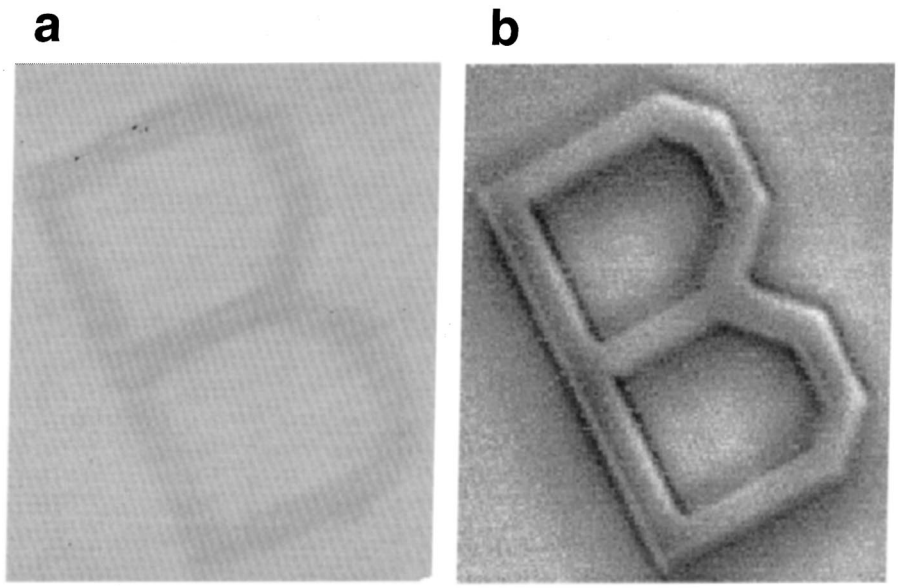

Fig. 12. a, SXM image of a letter structure in 2-μm-thick PMMA in bright-field mode. The field of view is 20 μm $\times$ 20 μm, the pixel size is 100 nm $\times$ 100 nm, and the dwell time is 50 ms per pixel. The image contrast is 1.5%. b, Same structure in DIC mode with a contrast of 25%, proving that the x-ray DIC technique can also be applied to scanning transmission x-ray microscopy.

order-sorting aperture upstream of the sample blocks spurious diffraction orders of the two ZPs and extracts only the (1, 0) and (0, 1) wave fronts. A Si photodiode with a 50-μm aperture in front was placed on one flank of an interference fringe in order to be highly sensitive to shifts of the fringes related to optical path differences introduced by the raster-scanned specimen. On account of the off-axis alignment of the aperture diode, no central stop was introduced in the optical scheme to block the (0, 0) contribution.

Figure 10b shows a raster scan of the aperture detector across the first-order diffracted light of the TZP, demonstrating the strong phase modulation. For comparison a raster scan across a single ZP with the same parameters generated under identical conditions is shown in Fig. 10a. The phase modulation leads to an intensity variation of more than 10^4, as plotted in Fig. 11.

Figure 12 is a SXM image of the same PMMA structure as that in Fig. 6d taken at 4-keV photon energy with a dwell time of 50 ms/pixel and a pixel size of 100 nm. As in the full-field imaging setup, we observe a contrast of more than 25% compared with 1.5% in bright-field imaging mode, demonstrating that this DIC technique can also effectively be applied to SXMs. This technique is therefore the first differential imaging technique that is suited for *both* types of x-ray microscope.

4. DISCUSSION AND CONCLUSION

In this contribution, we have described high-resolution x-ray imaging using differential interference contrast (DIC) with two complementary microscopy geometries: full-field imaging and scanning types.

We proved with both microscope setups that the x-ray DIC method using twin zone plates (TZPs) leads to a significant increase in image contrast. Different from the Nomarski DIC method for visible light, this technique, using monochromatic light, is capable of providing quantitative specimen information in combination with, for example, x-ray absorption near-edge spectroscopy or x-ray fluorescence. The image formation is on line and does not require after-the-fact data analysis to extract the phase information. The visible image depends on the orientation of the specimen with respect to the wave-front shear direction. The directionality ("shadowing") can be eliminated by acquiring images at different specimen orientations and using data processing.[54]

In addition, the x-ray DIC using TZPs is easy to set up and can be used in any standard transmission x-ray microscope with no other precaution than that for a single zone plate (ZP). Though the experiments here were performed at 4-keV photon energy, this technique can be extended to any photon energy range, where ZPs with appropriate imaging performance can be generated (currently approximately 0.03–30 keV).

A difficulty with this technique is the fabrication of the TZP, especially the need for accuracy in aligning the two ZPs, which currently limits the achievable spatial resolution. Higher-resolving TZPs are expected with the application of new x-ray lithography and nanostructuring techniques. Combination of both ZPs of the TZP into a single ZP would solve this problem and is in preparation.

ACKNOWLEDGMENTS

We thank Murielle Salomé, Ulrich Neuhaeusler, Robert Baker, and Alexei Barinov for all their help and assistance, which made these experiments possible and successful. We especially acknowledge Lionel André, Gilles Berruyer, Franck Demarcq, Francois Durel, and Gerard Rostaing for their engineering support. We thank Pambos Charalambous for providing the W Siemens star. Very special thanks are given to Sebastian Oestreich for his contributions to the full-field imaging microscope at ID21.

Address correspondence to B. Kaulich at kaulich @elettra.trieste.it.

REFERENCES

1. W. C. Röntgen, "On a new kind of rays," Nature (London) **53**, 274–276 (1896).
2. H. Wolter, "Spiegelsysteme streifenen Einfalls als abbildende Optiken für Röntgenstrahlen," Ann. Phys. (Leipzig) **6**, 94–114 (1952).
3. J. Kirz, C. Jacobsen, and M. Howells, "Soft x-ray microscopes and their biological applications," Q. Rev. Biophys. **28**, 33–130 (1995).
4. G. Schmahl, D. Rudolph, P. Guttmann, G. Schneider, J. Thieme, and B. Niemann, "Phase contrast studies of biological specimen with the x-ray microscope at BESSY," Rev. Sci. Instrum. **66**, 1282 (1995).
5. C. Jacobsen and J. Kirz, "X-ray microscopy with synchrotron radiation," Nat. Struct. Biol. **5** (suppl.), 650–653 (1998).
6. W. Meyer-Ilse, H. Medecki, L. Jochum, E. Anderson, D. Attwood, C. Magowan, R. Balhorn, M. Moronne, D. Rudolph, and G. Schmahl, "New high-resolution zone-plate microscope at beamline 6.1 of the ALS," Synchr. Radiat. News **8**, 29–33 (1995).
7. R. Medenwaldt and E. Uggerhøj, "Description of an x-ray microscope with 30 nm resolution," Rev. Sci. Instrum. **69**, 2974–2977 (1998).
8. D. Sayre, J. Kirz, R. Feder, D. M. Kim, and E. Spiller, "Transmission microscopy of unmodified biological materials: comparative radiation dosages with electrons and ultrasoft x-ray photons," Ultramicroscopy **2**, 337–349 (1977).
9. D. Rudolph, G. Schmahl, and B. Niemann, "Amplitude and phase contrast in x-ray microscopy," in *Modern Microscopies, Techniques and Applications*, A. Michette and P. Duke, eds. (Plenum, London, 1990), p. 59.
10. G. Schneider, "Cryo x-ray microscopy with high spatial resolution in amplitude and phase contrast," Ultramicroscopy **75**, 85–104 (1998).
11. G. Schmahl, D. Rudolph, and P. Guttmann, "Phase contrast x-ray microscopy experiments at the BESSY storage ring," in *X-ray Microscopy II*, D. Sayre, M. Howells, J. Kirz, and H. Rarback, eds., Vol. 56 of Springer Series in Optical Science (Springer-Verlag, Berlin, 1988), pp. 228–232.
12. G. Schmahl, D. Rudolph, G. Schneider, P. Guttmann, and B. Niemann, "Phase contrast x-ray microscopy studies," Optik (Stuttgart) **97**, 181–182 (1994).
13. F. Zernike, "How I discovered phase contrast," Science **121**, 345–349 (1995).
14. G. R. Morrison, A. R. Hare, and R. E. Burge, "Transmission microscopy with soft x-rays," in *Proceedings of the Institute of Physics Electron Microscopy and Analysis Group Conference* (Institute of Physics, Bristol, UK, 1987), pp. 333–336.
15. G. R. Morrison and B. Niemann, "Differential phase contrast x-ray microscopy," in *X-ray Microscopy and Spectromicroscopy*, J. Thieme, G. Schmahl, D. Rudolph, and E. Umbach, eds. (Springer-Verlag, Berlin, 1998), pp. I-85–I-94.
16. H. N. Chapman, C. Jacobsen, and S. Williams, "Applications of a CCD detector in scanning transmission x-ray microscope," Rev. Sci. Instrum. **66**, 1332–1334 (1995).
17. H. Rose, "Nonstandard imaging methods in electron microscopy," Ultramicroscopy **2**, 251–267 (1977).
18. M. Waddel and J. N. Chapman, "Linear imaging of strong phase objects using asymmetrical detectors in STEM," Optik (Stuttgart) **54**, 251–267 (1999).
19. F. Polack, D. Joyeux, J. Svaloš, and D. Phalippou, "Applications of wavefront division interferometers in soft x rays," Rev. Sci. Instrum. **66**, 2180 (1995).
20. D. Joyeux, F. Polack, and D. Phalippou, "An interferometric determination of the refractive part optical constants for carbon and silver across absorption edges," Rev. Sci. Instrum. **70**, 2921 (1999).
21. T. J. Davis, T. E. Gureyev, D. Gao, A. W. Stevenson, and S. W. Wilkins, "X-ray image contrast from a simple phase object," Phys. Rev. Lett. **74**, 3173–3176 (1995).
22. T. J. Davis, D. Gao, T. E. Gureyev, A. W. Stevenson, and S. W. Wilkins, "Phase-contrast imaging of weakly absorbing materials using hard x-rays," Nature (London) **373**, 595–598 (1995).
23. B. E. Allman, P. J. McMahon, J. B. Tiller, K. A. Nugent, D. Paganin, A. Barty, I. McNulty, S. P. Frigo, Y. Wang, and C. C. Retsch, "Noninterferometric quantitative phase imaging with soft x rays," J. Opt. Soc. Am. A **17**, 1732–1743 (2000).
24. A. Snigirev, I. Snigireva, V. Kohn, S. Kuznetsov, and I. Schelokov, "On the possibilities of x-ray phase contrast microimaging by coherent high-energy synchrotron radiation," Rev. Sci. Instrum. **66**, 5486–5492 (1995).
25. I. McNulty, "The future of x-ray holography," Nucl. Instrum. Methods Phys. Res. A **347**, 170–176 (1994).
26. S. W. Wilkins, T. E. Gureyev, D. Gao, A. Pogany, and A. W. Stevenson, "Phase-contrast imaging using polychromatic hard x-rays," Nature (London) **384**, 335–338 (1996).
27. P. Cloetens, R. Barrett, J. Baruchel, J.-P. Guigay, and M. Schlenker, "Phase objects in synchrotron radiation hard x-ray imaging," J. Phys. D **29**, 133–146 (1996).
28. P. Cloetens, M. Salome-Pateyron, J.-I. Bufiere, G. Peix, J. Baruchel, F. Peyrin, and M. Schlenker, "Observation of microstructure and damage in materials by phase sensitive radiography and tomography," J. Appl. Phys. **81**, 5878–5886 (1997).
29. A. Momose, T. Takeda, and Y. Itai, "Phase-contrast x-ray computed tomography for observing biological specimens and organic materials," Rev. Sci. Instrum. **66**, 1434–1436 (1995).
30. A. Momose, T. Takeda, Y. Itai, and K. Hirano, "Phase-contrast x-ray microtomography: application to human cancerous tissues," in *X-Ray Microscopy and Spectromicroscopy*, J. Thieme, G. Schmahl, D. Rudolph, and E. Umbach, eds. (Springer-Verlag, Berlin, 1998), pp. II-207–II-211.
31. R. F. Stevens, "Zone plate interferometer," J. Mod. Opt. **35**, 75–79 (1988).
32. R. M. Smartt, "Zone plate interferometer," Appl. Opt. **13**, 1093–1099 (1974).
33. M. V. R. K. Murty, "Common path interferometer using Fresnel zone plates," J. Opt. Soc. Am. A **53**, 568–570 (1963).
34. F. Broder-Burztyn and D. Malacara-Hernandez, "Holographic interferometer to test optical surfaces," Appl. Opt. **14**, 2280–2282 (1975).
35. J. C. Fouere and C. Roychoudhuri, "A holographic, radial and lateral shear interferometer," Opt. Commun. **12**, 29–31 (1974).
36. H. Tanigawa, K. Nakajima, and S. Matsuura, "Modified zone-plate interferometer for testing aspheric surfaces," Opt. Acta **27**, 1327–1334 (1980).
37. V. Moreno, M. V. Perez, and J. Linares, "Zone plates with initial phase shift for optical sensing," J. Mod. Opt. **39**, 2039–2052 (1992).
38. T. Wilhein, B. Kaulich, and J. Susini, "Two zone plate interference contrast microscopy at 4 keV photon energy," Opt. Commun. **193**, 19–26 (2001).
39. E. Di Fabrizio, F. Romanato, M. Gentili, S. Cabrini, B. Kaulich, J. Susini, and R. Barrett, "Multilevel x-ray zone plates," Nature (London) **401**, 895 (1999).
40. T. Wilhein, B. Kaulich, E. Di Fabrizio, S. Cabrini, F. Romanato, and J. Susini, "Differential interference contrast x-ray microscopy with submicron resolution," Appl. Phys. Lett. **78**, 2079–2081 (2001).
41. J. Susini and R. Barrett, "The x-ray microscopy facility project at the ESRF," in *X-Ray Microscopy and Spectromicroscopy*, J. Thieme, G. Schmahl, D. Rudolph, and E. Umbach, eds. (Springer-Verlag, Berlin, 1998), pp. I-45–I-54.
42. See, for example, http://www.esrf.fr.
43. A. G. Michette, *Optical Systems for Soft X-Rays* (Plenum, New York, 1986).
44. D. Attwood, *Soft X-Rays and Extreme Ultraviolet Radiation* (Cambridge U. Press, Cambridge, UK, 1999).
45. Z. Jaroszewicz, V. Moreno, and S. Bara, "Interferometric alignment using parabolic and off-axis conical zone plates," Appl. Opt. **29**, 4614–4617 (1990).
46. M. Born and E. Wolf, *Principles of Optics* (Pergamon, Oxford, UK, 1991).
47. S. Oestreich, B. Kaulich, and J. Susini, "Single-movement fixed-exit channelcut x-ray monochromator based

on pro-filed surfaces," Rev. Sci. Instrum. **70**, 1921–1925 (1999).
48. B. Kaulich, T. Wilhein, S. Oestreich, M. Salome, R. Barrett, J. Susini, E. Di Fabrizio, M. Gentili, and P. Charalambous, "Feasibility of transmission x-ray microscopy at 4 keV with spatial resolutions below 150 nm," Appl. Phys. Lett. **75**, 4061–4063 (1999).
49. M. Pateyron, F. Peyrin, A. M. Laval-Jeantet, P. Spanne, P. Cloetens, and G. Peix, "3D microtomography of cancerous bone samples using synchrotron radiation," in *Medical Imaging 1996: Physics of Medical Imaging,* R. L. Van Metterand and J. Beuel, eds., Proc. SPIE **2708**, 417–426 (1996).
50. M. Salomé, F. Peyrin, P. Cloetens, C. Odet, A. M. Laval-Jeantet, J. Baruchel, and P. Spanne, "A synchrotron radiation microtomography system for the analysis of trabecular bone samples," Med. Phys. **26**, 2194–2204 (1999).
51. E. Zeitler and M. G. R. Thomson, "Scanning electron microscopy," Optik (Stuttgart) **31**, 258–280 (1970).
52. G. R. Morrison, "Some aspects of quantitative x-ray microscopy," in *X-Ray Instrumentation in Medicine and Biology, Plasma Physics, Astrophysics, and Synchrotron Radiation*, R. Benattar, ed., Proc. SPIE **1140**, 41–49 (1989).
53. R. Barrett, B. Kaulich, M. Salome, and J. Susini, "Current status of the scanning x-ray microscope at the ESRF," in *X-Ray Microscopy*, W. Meyer-Ilse, T. Warwick, and D. Attwood, eds., AIP Conf. Proc. **507**, 458–463 (1999).
54. C. Preza, "Rotational-diversity phase estimation from differential-interference-contrast microscopy images," J. Opt. Soc. Am. A **17**, 415–424 (2000).